Effect of Carbon Supports on Electrocatalytic Reactivity of Au–Pd Core–Shell Nanoparticles

6 AUTHORS, INCLUDING:

Veronica Celorrio
University of Bristol
31 PUBLICATIONS **208** CITATIONS

SEE PROFILE

Daniela Plana
Keele University
29 PUBLICATIONS **237** CITATIONS

SEE PROFILE

Rafael Moliner
Spanish National Research Council
183 PUBLICATIONS **3,543** CITATIONS

SEE PROFILE

M.J. Lázaro
Spanish National Research Council
**217** PUBLICATIONS **4,079** CITATIONS

SEE PROFILE

Effect of Carbon Supports on Electrocatalytic Reactivity of Au−Pd Core−Shell Nanoparticles

V. Celorrio,[†] M. G. Montes de Oca,[‡] D. Plana,[‡] R. Moliner,[†] M. J. Lázaro,[†] and D. J. Fermín*,[‡]

[†]Instituto de Carboquímica (CSIC), Miguel Luesma Castán 4, 50018 Zaragoza, Spain
[‡]School of Chemistry, University of Bristol, Cantocks Close, Bristol BS8 1TS, U.K.

ABSTRACT: The role of particle-substrate interactions on the reactivity of bimetallic nanostructures is investigated in the case of Au−Pd core−shell nanoparticles supported on Vulcan XC-72R (Vulcan). Core−shell nanostructures (CS) featuring 19 nm Au cores and Pd shells with thicknesses between ca. 1 and 10 nm were synthesized by controlled colloidal methods and subsequently incorporated in the carbon support. X-ray diffraction, energy dispersive X-ray analysis, and high resolution transmission electron microscopy confirmed the CS nature of the nanostructures, which remain unaffected upon incorporation onto the carbon matrix. Their electrochemical properties toward CO and HCOOH electro-oxidation were studied, using cyclic voltammetry and chronoamperometry. The results show that the CO stripping potential becomes independent of the average Pd lattice strain in the case of Vulcan supported CS. This behavior is significantly different to the trend observed in CS assemblies at In-doped SnO$_2$ electrodes. Formic acid oxidation is also strongly affected not only by the thickness of the Pd nanoshell but also by the support. These reactivity trends are discussed in terms of strain (geometric) effects, CS crystalline structure, and substrate effects on the onset potential for the formation of oxygenated species at the catalyst surface.
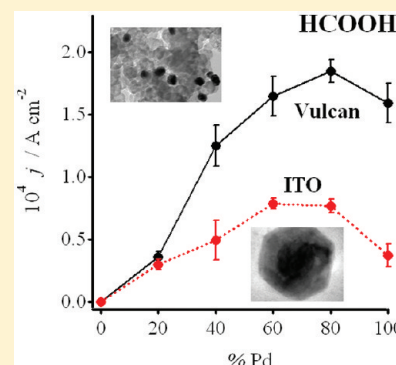
1. INTRODUCTION

Highly porous carbon supports play a key role on the performance of fuel cell electrocatalysts. Some of the key requirements for electrocatalysts supports include (i) large specific surface area for achieving high metal dispersions, (ii) good electrical conductivity, (iii) suitable pore size for optimum diffusion of reactants and byproduct to and from the catalyst, (iv) good corrosion resistance, and (v) low cost.[1,2] Carbon black is the most commonly used material for these applications, in particular Vulcan XC-72R, which combines good electrical conductivity and high surface area.[3] Conventional methods for preparing metallic nanostructures supported on porous carbon matrices involve the impregnation of the metal precursor followed by chemical reduction. In this type of approach, the structure and surface composition of carbon supports can exert a strong influence on the growth of metallic centers, affecting key parameters such as size, morphology, size distribution, stability, and dispersion, which in turn can affect catalytic activity.[4−7] However, investigations on the role of substrate on the reactivity of already formed nanostructures, e.g., via colloidal synthesis, are relatively scarce.[8] Such an approach would allow decoupling effects of the support on particle growth from specific chemical interactions linked to the reactivity of the metallic centers, i.e., any effect observed in the catalytic activity could be directly linked to the support on the electrochemical activity and not to particle size, distribution, etc.

The direct formic acid fuel cell (DFAFC) is emerging as a rather attractive alternative to more established systems such as hydrogen (HFC) and direct methanol fuel cells (DMFC). The latter two technologies still face important drawbacks such as hydrogen generation, storage and distribution, or the high toxicity of methanol.[9−11] Although formic acid exhibits a lower volumetric energy density than methanol (2086 Wh L^{-1} vs 4690 Wh L^{-1}), the smaller crossover through the membrane allows the use of high fuel concentrations.[12−14]

The electro-oxidation of formic acid has been investigated at catalytically active surfaces[12,15−21] on which a dual pathway mechanism has been proposed.[22] It is generally agreed that HCOOH oxidation at Pt surfaces undergoes the formation of adsorbed CO intermediates, requiring the presence of surface oxygenated species to proceed to the formation of CO$_2$. However, on Pd it occurs primarily via a direct pathway, avoiding the formation of CO as an intermediate. Nevertheless, Pd and Pd-based catalysts undergo substantial deactivation under operational conditions, and a discussion has emerged in the literature regarding the long-term stability of Pd catalysts in direct formic acid fuel cells.[23−26] Yu and Pickup have recently concluded that deactivation is due to CO poisoning, occurring at longer time-scales than on Pt centers.[14]

We have recently proposed that the interaction between CO and Pd can be significantly affected by the average lattice strain, as determined by selected area electron diffraction patterns (SADPs).[27] Pd nanoshells grown on Au nanoparticles exhibit a

thickness dependence lattice strain in the range of 1 to 10 nm, which can be described in terms of the Matthew's model.[28] Other studies, employing a slightly different synthesis method, have shown that Pd monolayers on Au cores exhibit Shockley partial dislocations, while further layers mainly present stacking faults.[29] Changes in the average lattice strain affect the position of the d-band center, which plays a crucial role on the interaction with organic adsorbates.[30,31] Pioneering works in this area were based on the pseudomorphic growth of Pd layers on Au single crystal surfaces.[32−34] Recent studies on Au−Pd core−shell[35] and alloyed nanoparticles[16,36] supported on various carbon matrices have also suggested enhanced catalytic activity with respect to pure Pd catalysts.

In the present work, we attempt to elucidate the effect of a particular carbon support, Vulcan XC-72R (Vulcan), on the electrocatalytic activity of Au−Pd core−shell nanostructures (CS) toward CO and HCOOH oxidation. We systematically vary the thickness of the Pd shell in order to evaluate whether the so-called support effects counteract or enhance changes in reactivity induced by lattice strain. Electron microscopy and XRD analysis confirm that the adsorption of CS nanoparticles on Vulcan (CS/C) resulted in a homogeneous distribution of particles, without affecting their structure. Valuable insights into the effect of the support are established from comparisons with electrochemical behavior of the same CS nanoparticles assembled at In-doped SnO_2 electrodes. Voltammetric studies in sulfuric acid containing electrolytes indicate that, while CO coverage is affected by the average Pd thickness,[27] the stripping potential changes significantly only in the case of highly strained nanoshells supported on Vulcan. Furthermore, the deactivation rate during HCOOH oxidation at constant potential is slower on the carbon supported nanoparticles. The fact that we decouple the synthesis of the nanostructures from the preparation of the assemblies allows the identification of support effects on the reactivity of the system rather than on the structure or morphology of the metallic centers.

2. EXPERIMENTAL METHODS

2.1. Synthesis of the Core−Shell Nanoparticles Supported on Vulcan.
Pd nanoparticles (NPs) were prepared with a reaction mixture of $Na_2PdCl_6 \cdot 4H_2O$ and trisodium citrate under reflux and strong stirring for 4 h.[37,38] The synthesis of Au−Pd CS nanostructures involved a two step process initiated by the preparation of Au nanoparticles, employing trisodium citrate as a reducing and stabilizing agent. The second step was the Pd growth onto the as-grown Au cores by reduction of H_2PdCl_4, in the presence of ascorbic acid.[28,39] Pd thickness can be controlled by the amount of Pd precursor added in the second step.

The metallic nanostructures were supported on Vulcan XC-72R (Cabot), which consists of spherical particle aggregates, with sizes ranging from 30 to 60 nm. It has a relatively large specific surface area of 218 m^2 g^{-1} and a total pore volume of 0.41 cm^3 g^{-1}, presenting a mesoporous structure; however, it also contains a large number of micropores (30% of total surface area).[3] A set amount of the as received Vulcan powder was suspended and stirred during 48 h in controlled amounts of nanoparticle dispersions, calculated to obtain a total metal loading of 20 wt %. The as-prepared carbon-supported nanoparticle powders were filtered, washed with Milli-Q water, and dried at 60 °C overnight.

2.2. Characterization of Electrocatalysts.
The metal loading on the carbon support was controlled by monitoring the weight ratio of the nanoparticles versus that of Vulcan. The real loading was determined by energy dispersive X-ray (EDX) analysis using an Oxford Instruments ISIS 300, coupled to a JEOL JSM 5600LV scanning electron microscope. TEM images, for determination of the size and morphology, were obtained using a JEOL JEM 1200 EX MKI and the image analysis software Soft Imaging Systems GmbH analySIS 3.0. Samples for TEM were produced by placing 10 μL drops of the carbon supported catalysts dissolved in ethanol on a 3 mm diameter carbon-coated copper grid. Excess solution was absorbed with filter paper, and the sample was dried in air at room temperature. Average diameters and shell thicknesses of the core−shell structures were obtained from HR-TEM images of at least 200 nanoparticles per sample and their elementary composition was estimated from EDX measurements.[28]

High-angle annular dark-field scanning transmission electron microscopy (STEM-HAADF) images and EDX analysis were performed in a FEI Tecnai F30, equipped with a field emission gun working at 300 kV. EDX spectra were obtained with an energy dispersion of 0.5 eV per channel. Spatially resolved EDX analysis was used to analyze the chemical composition of each Au−Pd CS sample. Since each element has a characteristic energy edge, chemical profiles of each element can be plotted. This technique is known as spectrum-line or line-scan acquisition. The supported catalysts were also examined by powder X-ray diffraction (XRD) using a Bruker AXS D8 Advance diffractometer with a $\theta−\theta$ configuration and CuKα radiation. Scans were done for 2θ values between 20 and 100°. XRD patterns were compared to the Au and Pd reference patterns from the powder diffraction file (PDF), International Centre for Diffraction Data; the powder diffraction files used as reference were PDF 040784 and 461043, for Au and Pd, respectively.

2.3. Electrochemical Studies.
A two-compartment electrochemical cell was used, incorporating a Pt wire and KCl-saturated silver/silver chloride (KCl-saturated Ag/AgCl) as counter and reference electrodes, respectively. The reference and working electrodes were placed in different compartments connected by a Luggin capillary. All potentials were measured and are quoted with respect to the Ag/AgCl reference electrode. The electrochemical cell was placed in a Faraday cage to isolate it from environmental electronic noise. All measurements were carried out at room temperature, in aqueous solutions (Milli-Q, 18.2 MΩ cm resistivity) containing high purity 0.5 mol dm^{-3} sulfuric acid (H_2SO_4, 98%, Fisher). Solutions were purged with high purity argon, for at least 20 min prior to a series of experiments. Cyclic voltammograms were recorded with an Autolab PGSTAT30.

Catalyst inks were prepared by mixing 2 mg of the catalyst powder, 15 μL of Nafion dispersion (5 wt.%, Aldrich) and 500 μL of ultrapure water (Millipore Milli-Q system). A 40 μL aliquot of the ink was drop-cast onto a glassy carbon electrode (7 mm diameter) and dried. The working electrode was introduced into the electrochemical cell in a meniscus configuration. The electrochemical active areas of the catalysts were determined from the charges obtained in CO-stripping voltammograms, using charge densities obtained in previous work as normalization parameters.[27] These experiments were carried out by bubbling CO (99.97%, CK gas) through the electrolyte during 15 min, while the electrode was immersed in solution and held at −0.166 V. Argon was used to purge CO out from solution before running the stripping voltammetry, leaving only the CO adsorbed on Pd surface. The potential was

scanned between −0.20 and 1.0 V, at 0.02 V s^{-1}. HCOOH oxidation was studied by cyclic voltammetry and chronoamperometry. Cyclic voltammograms were recorded in 2 mol dm^{-3} HCOOH (98%, Fluka) and 0.5 mol dm^{-3} H$_2$SO$_4$ aqueous solutions between −0.2 and 1.0 V at 0.02 V s^{-1}. Chronoamperometric measurements were recorded in the same solution at 0.4 V for 900 s.

3. RESULTS AND DISCUSSION

3.1. CS Nanostructures Supported on Vulcan. Figure 1 shows characteristic TEM images of the various CS
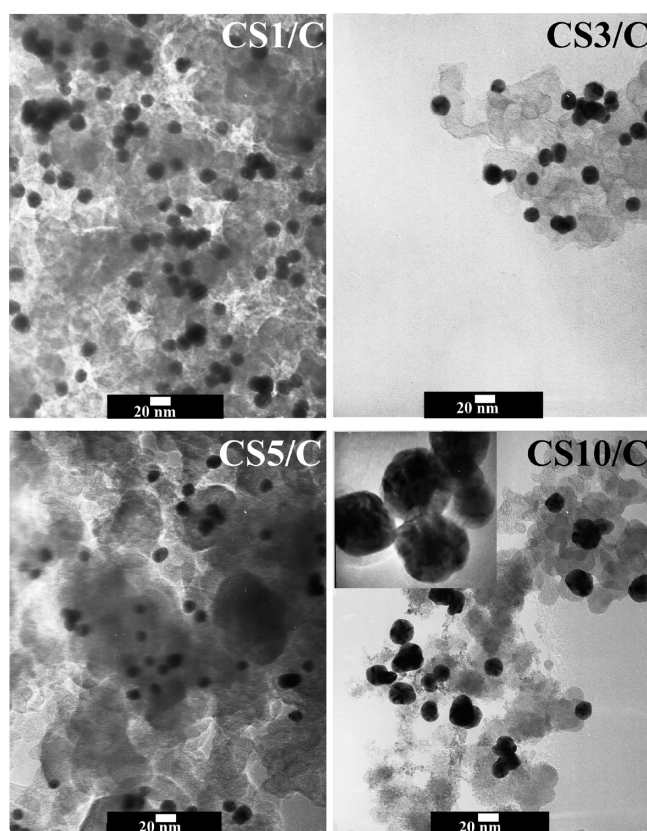
Figure 1. TEM images of the various CS nanoparticles supported on Vulcan. The inset in CS10 is an image with higher magnification, showing the contrast between the Au core and the Pd shell.

nanostructures supported on Vulcan. The images show a systematic increase in the particle size as the Pd atomic ratio with respect to Au content increases from 20 to 80%. CS nanoparticles are well dispersed in the carbon support, ensuring a high metal dispersion in the catalysts with very low density of aggregates. The average particle diameter (*D*) and shell thickness (*δ*) are consistent with those obtained from analysis of a large number of as-prepared (unsupported) nanoparticles.[28] Table 1 summarizes the average dimensions of particles as a function of Pd content, as well as the average metal loading of each catalyst as estimated from EDX. No metallic nanostructures with sizes significantly smaller than 20 nm are observed in any of the samples investigated, strongly suggesting that Pd nucleation occurs exclusively at the Au cores. The average atomic metal weight ratio obtained from EDX measurements corresponds very accurately to the composition of the synthesis bath, further confirming that the Pd precursor

Table 1. Average Diameter (*D*), Pd Thickness (*δ*), Au:Pd Weight Composition, and Metal Loading on the Vulcan Support

	D (nm)^a	*δ* (nm)^a	Au:Pd weight ratio	metal loading (wt %)
Au/C	19.3 ± 1.2		100:0	19.5 ± 1.2
CS1/C	21.8 ± 1.1	1.3 ± 0.1	81.3:18.7 ± 2.4	15.0 ± 1.9
CS3/C	24.7 ± 1.3	2.7 ± 1.0	61.9:38.1 ± 1.1	19.2 ± 2.1
CS5/C	29.5 ± 1.2	5.1 ± 0.9	42.2:57.8 ± 0.9	18.5 ± 2.9
CS10/C	38.9 ± 1.5	9.9 ± 1.1	17.9: 82.1 ± 0.7	17.5 ± 1.4
Pd/C	10.0 ± 1.8		0:100	18.4 ± 2.5

^{a}Values obtained after analysis of more than 200 as-prepared nanoparticles.[28]

is entirely reduced at the Au nanoparticles. The total metal loading in the catalysts are in the range of 15 to 20%.

The core−shell configuration of the nanostructures is demonstrated by the STEM-HAADF images of CS1 and CS5 shown in Figure 2, where a strong contrast is observed between
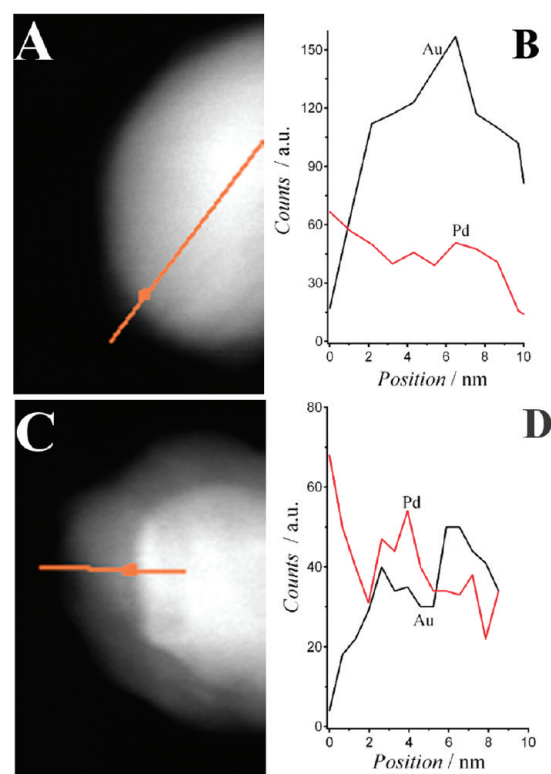

Figure 2. STEM-HAADF images and EDX intensity profile of CS1 (A,B) and CS5 (C,D) nanoparticles. The EDX intensity profile is obtained along the red line indicated in the corresponding STEM image.

the bright Au core and the more opaque Pd shell (Figure 2A,C). The intensity profiles produced by the line-scan analysis of Au−M*α* and Pd−L*α* X-rays along the line on the STEM-HAADF images are plotted in Figure 2B,D, for CS1 and CS5 nanoparticles, respectively. The EDX line-scan analysis confirmed that nanoparticles are composed of Au and Pd. The initial point of the scan is located at the particle edge, showing that the CS surface mainly contains Pd. The crossing over point in Figure 2B,D between the Au and Pd intensity lines, as Au content increases, agrees well with the Pd layer thickness determined from the difference in average diameter

between CS nanoparticles and the initial Au core. Although this analysis does not entirely exclude the possibility of a degree of metallic intermixing at the Au−Pd boundary layer (the spatial resolution of the technique is approximately 1 nm), it can be concluded that the surface of the CS nanoparticle is overwhelmingly composed of Pd. These results agree with previous reports, which conclude that, although there might be a degree of mixing in the first layer of Pd, high temperatures are required to observe a significant amount of alloying between Pd shells and Au cores.[29,40−42]

Figure 3 shows the powder X-ray diffractograms for the different catalysts. The Au/C sample features sharp diffraction
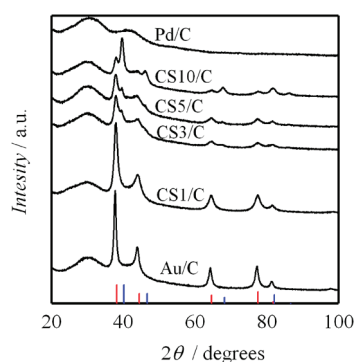

Figure 3. Powder XRD diffractograms of the various metallic nanostructures on the Vulcan support. Composition and dimension of the various samples are indicated in Table 1. The red lines at the bottom of the graph, at 38.1°, 44.4°, 64.6°, 77.5°, and 81.7°, indicate the standard Au diffraction pattern (PDF 040784), while the blue lines at 40.1°, 46.7°, 68.1°, 82.1° and 86.6° belong to Pd (PDF 461043).

peaks due to the well-defined polycrystalline structure of Au. The signals at 38.3°, 43.9°, 64.8°, 77.7°, and 81.5° are due to the (111), (200), (220), (311), and (222) planes of the face-centered cubic (fcc) gold phase, respectively. The highest diffraction peak can be seen at 38.3°, suggesting that Au nanoparticles have a strong (111) orientation. No clear diffraction peaks are observed for Pd/C sample, suggesting a poor crystalline structure of the monometallic nanoparticles. The presence of Au cores templates the growth of the Pd shells, allowing the progressive appearance of Pd diffraction peaks on the core−shell samples. The characteristic diffraction peak attributed to Pd(111) at $2\theta = 40.2°$ appears in CS3/C, CS5/C, and CS10/C samples, and its intensity increases with increasing Pd thickness. In addition to the peaks associated with the metallic nanostructures, all samples exhibit a broad peak at $2\theta = 26°$ that is characteristic of the plane (002) of graphite from Vulcan support.

The behavior of the XRD patterns in Figure 3 is consistent with a core−shell configuration of the metal nanoparticles, rather than with Au−Pd alloy formation. Alloyed particles have been shown to present peaks that shift from the position of the gold pattern to that of palladium as the Pd content increases, without shoulders or individual peaks being observed for each metal.[41,43] However, XRD patterns identical to Au are reported for very thin Pd shells on Au substrates,[44,45] with shoulder peaks appearing for increasingly thicker shells.[46] The tendency of Pd and Au to segregate, with Pd rich surfaces and Au cores, rather than forming alloys, has been reported.[47,48] Similar seeding growth methods as the one used here have been widely studied, with a variety of characterization techniques, such as

UV−vis spectroscopy, XRD, TEM (high resolution and dark field), EDX, elemental mapping, XANES, and EXAFS, have all confirmed the core−shell nature of Pd−Au nanostructures.[39,40,42,44,46,49,50] Our own previous work with selected area electron diffraction patterns (SADPs) provided a quantitative relationship between the average Pd shell thickness and its corresponding lattice strain induced by the Au core.[28] It has been established that in order for significant alloying to occur, the temperature needs to be increased considerably above room temperature (a range between 200 and 300 °C has been reported).[40,42] An important aspect of these results is that XRD patterns are almost identical to those reported for the same set of nanoparticles in the absence of Vulcan support.[27] This observation further confirms that the structure of the nanoparticles does not undergo any significant change, such as extensive aggregation or sintering, upon loading in the carbon matrix.

3.2. CO-Stripping from Vulcan Supported Nanostructures. Figure 4 contrasts the CO-stripping voltammetry of Pd/
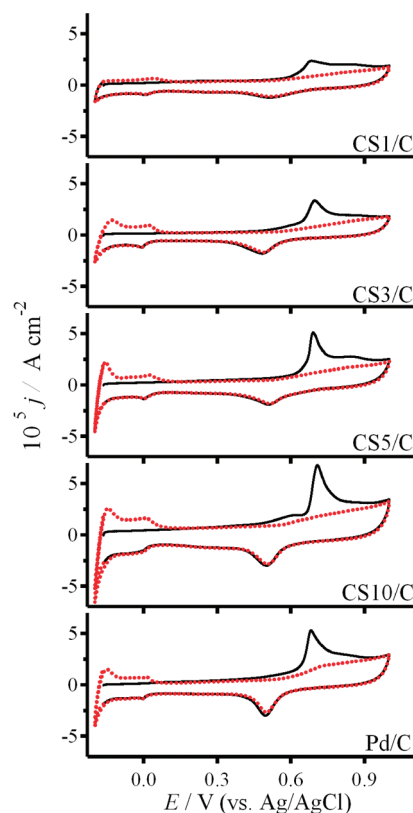
Figure 4. CO stripping voltammograms of the various nanostructures supported on Vulcan, in 0.5 mol dm^{-3} H$_2$SO$_4$ solution, at 0.02 V s^{-1}. The black full line corresponds to the first cycle, while the second cycle is displayed as a red dotted line.

C and the various CS/C materials as a function of the thickness of Pd shell. Hydrogen adsorption signals in the initial forward scan (solid line) appear completely suppressed due to the adsorbed CO blocking of the Pd active sites. The key feature of the forward scan is the CO stripping peak. The second cycle (dotted line) following CO stripping corresponds to the voltammogram of ultrathin Pd films in acidic media. Pd oxide formation and reduction are present at 0.6 V in the positive scan and 0.5 V in the negative scan, respectively. The peaks due to hydrogen adsorption and absorption are clearly developed in

the second cycle, suggesting a complete removal of CO in the initial forward scan. As expected, the hydrogen absorption signal at the negative end of the potential window exhibits a progressive increase with increasing Pd thickness. No detectable CO-stripping peak was found on the Au/C sample in the potential range studied (results not shown), which is consistent with the fact that CO does not adsorb on Au in acid solutions.[51]

The electroactive surface areas used for estimating the current density of the various catalysts in Figure 4 were calculated from the charge associated with the CO-stripping signal. In our previous studies, the average CO coverage as a function of Pd thickness was quantitatively determined employing electrostatic assemblies of CS nanostructures with controlled particle number density on ITO electrodes.[27] Employing the charge obtained from experiments in the absence of Vulcan support allows a more accurate determination of the active surface area. Obviously, this analysis is based on the assumption that the Vulcan support has little influence on the CO coverage at CS nanostructures. Other commonly used methods of determining the electroactive area of Pd involve oxide reduction or hydrogen signals. Taking the charge associated with the Pd oxide reduction, the effective surface area appears consistent to the values estimated from the CO-stripping charge, particularly in the case of larger Pd thickness. However, the use of hydrogen adsorption and PdO signals for estimating effective current densities is affected by the relatively large capacitive currents of the carbon-supported catalysts. All current densities presented in this work are normalized by the electrochemical active area of Pd obtained for each individual electrode as described above. On average, the electroactive areas are found to be between 6.2 and 8.5 cm^2, for the CS10/C and the CS1/C samples, respectively. It should also be mentioned that the average active surface area increases not only with increasing Pd thickness (geometric factor) but also due to an increase in the average roughness factor.[28]

One of the most important observations from Figure 4 is related to the position of the CO stripping peak as a function of the nanoparticle composition. Pd/C catalyst shows a CO-stripping peak potential at 0.69 V, following the common behavior described in the literature for these catalysts.[45,52] The potential at which CO stripping occurs is similar on all CS/C catalysts, although a small pre-peak is observed on the CS10/C sample. This feature is probably due to oxidation of CO at defect sites associated with the high surface roughness of this catalyst;[28] the effect of step edges at Pd (111) surfaces on the kinetics of CO oxidation has been previously noted in the literature.[33] The weak dependence of the CO stripping potential on Pd thickness on the CS/C samples is rather different to the behavior observed at electrostatically adsorbed CS nanoparticles on ITO electrodes (CS/ITO). A substantial shift of the CO-stripping peak toward more positive potential was observed upon decreasing Pd thickness on CS/ITO assemblies.[27] *This observation points toward a clear change in the particle reactivity induced by Vulcan support.* The origin of this change in reactivity is most likely related to the effect of the support on the generation of oxygen-containing groups at Pd surfaces, which is the initial step in both the formation of Pd oxides and CO stripping. It should also be noted that the onset potential of Pd oxide formation also exhibits a significantly weaker dependence on Pd thickness on CS/C with respect to CS/ITO. As an interesting comparison, Hayden et al. reported a strong increase of the potentials for CO stripping and oxide

formation with decreasing Pt center sizes supported on TiO$_2$, while this shift appears attenuated when supported on carbon.[53] We propose that the carbon support affects the structure of the water layer at the catalyst surface, which manifests itself by a common onset potential for the formation of oxygenated species at all CS nanoparticle surfaces supported on Vulcan. Although the mechanisms of water (and other oxygenated species such as hydroxides) adsorption on carbon surfaces is still under debate, it is clear that surface chemistry plays an important role.[54] The formation of water clusters of between 4 and 12 molecules, for example, has been reported to enhance adsorption in graphitic nanopores, changing the chemical affinity of the surface, as well as limiting the freedom of motion of the water molecules at the surface.[55] The role of water orientation on the properties of liquid/solid interfaces, and the influence of potential on the adopted configuration of water molecules at the surface has been reported; in the case of RuO$_2$, for example, water can be adsorbed through hydrogen bonds at reductive potentials, mainly as hydroxide linked through the oxygen atoms at intermediate potentials and forms a double water layer with closely packed oxygen at potentials just below oxygen evolution.[56] The effect of water orientation on electrochemical reactions has also attracted attention, with nitrobenzene reactions on Au electrodes being very dependent on whether water is adsorbed through the hydrogen or the oxygen atom at the electrode surface, for example.[57]

The average stripping charge density (CO coverage) exhibits a systematic decrease with decreasing Pd thickness in the CS containing catalysts. The fact that this parameter is used in the normalization of the current density prevents us from establishing quantitative relationships. However, this trend is qualitatively consistent with our previous studies on CS/ITO assemblies, revealing strain-induced effects on the interaction between Pd and CO.[27,28] *Consequently, it can be concluded that the CO coverage on Vulcan supported CS nanoparticles is determined by the lattice strain of Pd layer, while carbon support has a clear effect on the surface oxidation potential.*

3.3. Oxidation of Formic Acid. Figure 5 shows cyclic voltammograms recorded at room temperature for Pd and Au–Pd CS supported on Vulcan in 2 mol dm^{-3} HCOOH and 0.5 mol dm^{-3} H$_2$SO$_4$. Formic acid oxidation starts at −0.1 V and continues until it reaches a maximum in the positive scan at 0.3 V. A slight shift of the current peak toward more negative potentials is observed with increasing Pd content, reaching a value of 0.2 V for Pd/C. The drop in the current densities at more positive potentials is associated with the Pd oxide formation. In the backward scan, the surface remains inactive until the Pd oxide reduction takes place. The current densities for the negative and positive scans were nearly identical, while consecutive scans were highly reproducible (results not shown), indicating a low tendency for poisoning of electrode surfaces via adsorbed intermediates.[32]

The currents are similar for CS with thick Pd shells and pure Pd NPs, while they are significantly lower for the thinnest Pd shell (CS1/C). A similar trend was reported in the case of CS/ITO assemblies.[27] The rationale behind these observations is yet to be fully clarified. In the seminal work by Baldauf and Kolb on epitaxial Pd layers at Au single crystal electrodes, a very weak dependence of the HCOOH oxidation current was observed with Pd thickness.[32] However, the reactivity of Pd/Au(100) appears significantly higher than on Pd/Au(110) and Pd/Au(111). We can tentatively correlate the high currents observed on the thicker Pd layers with the appearance of the
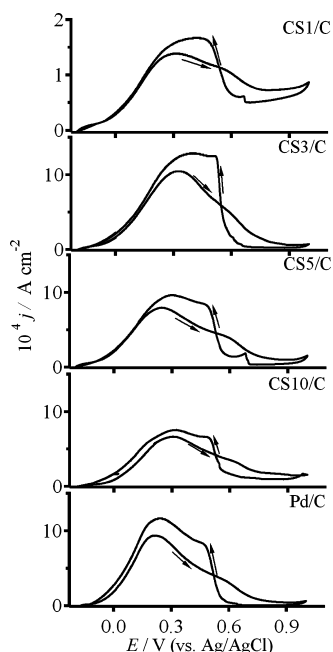
Figure 5. Cyclic voltammograms of the various nanostructures supported on Vulcan in the presence of 2 mol dm^{-3} HCOOH and 0.5 mol dm^{-3} H$_2$SO$_4$, at 0.02 V s^{-1}.

more reactive crystal planes in XRD patterns (see Figure 3). However, it is important to highlight the fact that our observations are qualitatively different to other reports in the literature.[45,58,59]

Although particle size effects can be significant in HCOOH oxidation, the results obtained here present the opposite trend to that established in previous works. Catalytic activity toward HCOOH oxidation is heavily affected by size when using particles below 10 nm and increases with decreasing size.[20,60] All particles used in this work are 10 nm or larger, and the catalytic activity increases with increasing particle size. Additionally, size effects have been recently linked to the appearance of crystal phases in the Pd nanoparticles, which agrees with our tentative explanations above.[20,27]

Figure 6 compares chronoamperometric transients at 0.40 V in the HCOOH containing electrolyte solution. As Au/C exhibited negligible activity for formic acid electro-oxidation under these experimental conditions, it was not included in the graph. All of the transients are characterized by a decay of the
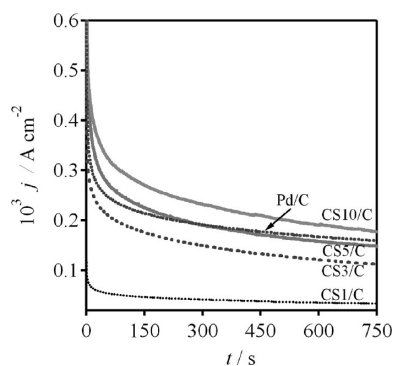
Figure 6. Chronoamperometric transients of Pd and CS catalysts supported on Vulcan at 0.40 V, in 2 mol dm^{-3} HCOOH and 0.5 mol dm^{-3} H$_2$SO$_4$.

current with time. This current decay is significantly stronger than expected for diffusion controlled process, suggesting that the origin of this process is the deactivation of the catalyst active sites. The apparent deactivation rate is rather similar for all of the samples, suggesting that the deactivation mechanism is not affected by the catalyst structure. However, the results show a clear increase of the reactivity toward formic acid oxidation with increasing Pd thickness.

The effect of support on the reactivity toward HCOOH oxidation is exemplified in Figure 7. The current density of
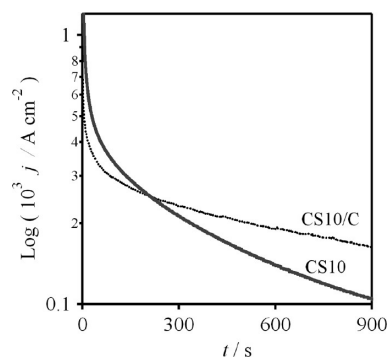

Figure 7. Comparison of transients associated with HCOOH oxidation on CS10 nanoparticles assembled at ITO (CS10/ITO) and supported on Vulcan (CS10/C), at 0.40 V. The composition of the electrolyte solution can be found in the caption of Figure 6.

CS10/ITO is slightly higher than at CS10/C at short times. However, *the deactivation rate of the carbon supported nanoparticles is significantly slower than on CS10/ITO assemblies.* The same behavior was observed for all CS and Pd nanostructures, suggesting that Vulcan support increases the catalyst tolerance toward poisoning intermediates. This effect could be related to the promotion of oxygenated species at Pd shells induced by Vulcan support, although further investigation is required in order to elucidate this trend. As mentioned above, it has been already demonstrated that a CO-like intermediate can be only oxidatively removed from the active sites by oxygen-containing species on a neighboring surface site.[18] Larsen et al. also concluded that the chronoamperometric activity of carbon supported Pd nanoparticles is higher than that of unsupported catalysts.[16] However, unlike the previously mentioned work, our studies are not affected by differences in particle size and dispersion.

Figure 8 compares the average formic acid oxidation current density obtained after 750 s at 0.40 V, for the various CS and Pd nanoparticles supported on Vulcan or assembled on modified ITO electrodes.[27] As mentioned previously, the current density associated with HCOOH strongly increases with increasing Pd thickness, probably due to the formation of highly reactive crystal facets on the thicker shells, as seen through XRD patterns in Figure 3. Although CS/ITO and CS/C exhibit similar trends, the current densities obtained for the carbon-supported nanoparticles are significantly higher, particularly for the pure Pd NPs and those CS nanoparticles with thicker Pd layers. As mentioned above, this behavior is connected to the slower deactivation rate of the catalytic active sites in the presence of carbon support. Consequently, the overall activity of the catalysts strongly depends on the composition/structure of the metallic nanostructures, while
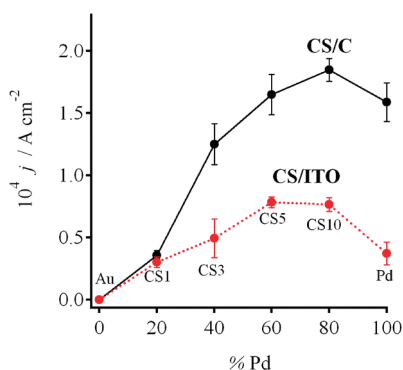
Figure 8. Current density at 750 s associated with HCOOH oxidation at 0.40 V on the various metallic nanostructures assembled on ITO (red) and supported on Vulcan (black). See caption of Figure 6 for the composition of the electrolyte solution.

the support plays an important role on the accumulation of intermediates at the active sites.

4. CONCLUSIONS

The reactivity of Au−Pd CS nanostructures toward CO and HCOOH electro-oxidation is not only determined by the composition and structure of Pd overlayer but also by interaction with the support. The approach described in this report is based on the synthesis of CS nanoparticles by colloidal methods with accurate control over the size and Pd thickness. The latter parameter strongly affect the average lattice strain of the Pd overlayer.[28] These nanoparticles are subsequently incorporated in Vulcan with a controlled total metal loading and without compromising the nanoparticle structure. Detailed analysis of the responses associated with CO striping in acid solution, employing independent CO coverage measurements at assemblies with control particle number density,[27] allows estimating the electrochemical active area of the nanoparticles supported on Vulcan.

Analysis of the CO stripping voltammograms in acid solution concluded that the CO coverage is strongly linked with the average lattice strain of CS nanoparticles, while the carbon support affects the onset potential for CO oxidation. In particular, the CO stripping peak potential on CS1/ITO[27] is shifted by approximately 100 mV toward more negative potentials on CS1/C. We propose that this shift in the oxidation potential is related to the structure of the water layer around CS/C structures, which decreases the onset for the formation of oxygenated species at the Pd surface.

HCOOH oxidation also exhibits a strong dependence on the support. Our results confirm that the current density is dependent on the thickness of Pd shells, although the physical rational for this behavior is yet to be clarified.[27] However, nanoparticles supported on Vulcan exhibit a significantly slower deactivation rate in chronoamperometric measurements, in comparison to CS/ITO assemblies. Although further studies are required to fully uncover the role of the substrate in the catalytic activity of metal centers, we believe the approach highlighted here elucidates some important trends. More importantly, these trends are not related to the effect of the substrate in the structure of the metallic center; a limitation in studies featuring conventional impregnation methods followed by nucleation of the nanoparticles in the carbon matrix. We are extending this methodology in order to evaluate a series of carbon supports with different structures and functionalities.

AUTHOR INFORMATION

Corresponding Author
*Tel: +44 117 9288981. Fax: +44 117 9250612. E-mail: David.Fermin@bristol.ac.uk. Weblink: www.bristol.ac.uk/pt/electrochemistry.

Notes
The authors declare no competing financial interest.

REFERENCES

(1) Dicks, A. L. *J. Power Sources* **2006**, *156*, 128.
(2) Tang, S.; Sun, G.; Qi, J.; Sun, S.; Guo, J.; Xin, Q.; Haarberg, G. M. *Chin. J. Catal.* **2010**, *31*, 12.
(3) Lázaro, M. J.; Calvillo, L.; Celorrio, V.; Pardo, J. I.; Perathoner, S.; Moliner, R. In *Carbon Black: Production, Properties and Uses*; Sanders, I. J., Peeten, T. L., Eds.; Nova Science Publishers, Inc.: Hauppauge, NY, 2011; p 41.
(4) Kim, M.; Park, J.-N.; Kim, H.; Song, S.; Lee, W.-H. *J. Power Sources* **2006**, *163*, 93.
(5) Yu, X.; Ye, S. *J. Power Sources* **2007**, *172*, 133.
(6) Calvillo, L.; Celorrio, V.; Moliner, R.; Lázaro, M. J. *Mater. Chem. Phys.* **2011**, *127*, 335.
(7) Liu, H.; Song, C.; Zhang, L.; Zhang, J.; Wang, H.; Wilkinson, D. P. *J. Power Sources* **2006**, *155*, 95.
(8) Celorrio, V.; Montes de Oca, M. G.; Plana, D.; Moliner, R.; Lázaro, M. J.; Fermín, D. J. *Int. J. Hydrogen Energy*, **2011**. DOI:10.1016/j.ijhydene.2011.12.014.
(9) Lamy, C.; Lima, A.; LeRhun, V.; Delime, F.; Coutanceau, C.; Léger, J.-M. *J. Power Sources* **2002**, *105*, 283.
(10) Edwards, P. P.; Kuznetsov, V. L.; David, W. I. F.; Brandon, N. P. *Energy Policy* **2008**, *36*, 4356.
(11) McNicol, B. D.; Rand, D. A. J.; Williams, K. R. *J. Power Sources* **1999**, *83*, 15.
(12) Huang, Y.; Zhou, X.; Liao, J.; Liu, C.; Lu, T.; Xing, W. *Electrochem. Commun.* **2008**, *10*, 621.
(13) Jeong, K.-J.; Miesse, C. M.; Choi, J.-H.; Lee, J.; Han, J.; Yoon, S. P.; Nam, S. W.; Lim, T.-H.; Lee, T. G. *J. Power Sources* **2007**, *168*, 119.
(14) Yu, X.; Pickup, P. G. *J. Power Sources* **2008**, *182*, 124.
(15) Ha, S.; Larsen, R.; Masel, R. I. *J. Power Sources* **2005**, *144*, 28.
(16) Larsen, R.; Ha, S.; Zakzeski, J.; Masel, R. I. *J. Power Sources* **2006**, *157*, 78.
(17) Huang, Y.; Liao, J.; Liu, C.; Lu, T.; Xing, W. *Nanotechnology* **2009**, *20*, 105604.
(18) Hu, C.; Bai, Z.; Yang, L.; Lv, J.; Wang, K.; Guo, Y.; Cao, Y.; Zhou, J. *Electrochim. Acta* **2010**, *55*, 6036.
(19) Wang, R.; Liao, S.; Ji, S. *J. Power Sources* **2008**, *180*, 205.
(20) Zhou, W.; Lee, J. Y. *J. Phys. Chem. C* **2008**, *112*, 3789.
(21) Zhang, L.; Lu, T.; Bao, J.; Tang, Y.; Li, C. *Electrochem. Commun.* **2006**, *8*, 1625.
(22) Capon, A.; Parsons, R. *J. Electroanal. Chem.* **1973**, *45*, 205.

6281

dx.doi.org/10.1021/jp211747a | *J. Phys. Chem. C* 2012, 116, 6275−6282

(23) Jung, W. S.; Han, J.; Yoon, S. P.; Nam, S. W.; Lim, T.-H.; Hong, S.-A. *J. Power Sources* **2011**, *196*, 4573.

(24) Yu, X.; Pickup, P. G. *Electrochem. Commun.* **2009**, *11*, 2012.

(25) Yu, X.; Pickup, P. G. *J. Power Sources* **2009**, *187*, 493.

(26) Zhou, Y.; Liu, J.; Ye, J.; Zou, Z.; Ye, J.; Gu, J.; Yu, T.; Yang, A. *Electrochim. Acta* **2010**, *55*, 5024.

(27) Montes de Oca, M. G.; Plana, D.; Celorrio, V.; Lázaro, M. J.; Fermín, D. J. *J. Phys. Chem. C* **2012**, *116*, 692.

(28) Montes de Oca, M. G.; Kumarakuru, H.; Cherns, D.; Fermín, D. J. *J. Phys. Chem. C* **2011**, *115*, 10489.

(29) Ding, Y.; Fan, F.; Tian, Z.; Wang, Z. L. *J. Am. Chem. Soc.* **2010**, *132*, 12480.

(30) Alcaide, F.; Álvarez, G.; Cabot, P. L.; Grande, H.-J.; Miguel, O.; Querejeta, A. *Int. J. Hydrogen Energy* **2011**, *36*, 4432.

(31) Xu, J. B.; Zhao, T. S.; Shen, S. Y.; Li, Y. S. *Int. J. Hydrogen Energy* **2010**, *35*, 6490.

(32) Baldauf, M.; Kolb, D. M. *J. Phys. Chem.* **1996**, *100*, 11375.

(33) El-Aziz, A. M.; Kibler, L. A. *J. Electroanal. Chem.* **2002**, *534*, 107.

(34) Kibler, L. A.; El-Aziz, A. M.; Kolb, D. M. *J. Mol. Catal. A: Chem.* **2003**, *199*, 57.

(35) Ruvinsky, P. S.; Prokin, S. N.; Zaikovskii, V. I.; Bernhardt, P.; Savinova, E. R. *Phys. Chem. Chem. Phys.* **2008**, *10*, 6665.

(36) Liu, Y.; Wang, L.; Wang, G.; Deng, C.; Wu, B.; Gao, Y. *J. Phys. Chem. C* **2010**, *114*, 21417.

(37) Turkevich, J.; Miner, R. S.; Babenkova, L. *J. Phys. Chem.* **1986**, *90*, 4765.

(38) Li, F.; Ciani, I.; Bertoncello, P.; Unwin, P. R.; Zhao, J. J.; Bradbury, C. R.; Fermin, D. J. *J. Phys. Chem. C* **2008**, *112*, 9686.

(39) Lu, L.; Wang, H.; Shiquan, S.; Zhang, H. *J. Mater. Chem.* **2002**, *12*, 156.

(40) Lee, A. F.; Baddeley, C. J.; Hardacre, C.; Ormerod, R. M.; Lambert, R. M.; Schmid, G.; West, H. *J. Phys. Chem.* **1995**, *99*, 6096.

(41) Nie, M.; Shen, P. K.; Wei, Z. *J. Power Sources* **2007**, *167*, 69.

(42) Hu, J.-W.; Li, J.-F.; Ren, B.; Wu, D.-Y.; Sun, S.-G.; Tian, Z.-Q. *J. Phys. Chem. C* **2007**, *111*, 1105.

(43) Lee, Y. W.; Kim, N. H.; Lee, K. Y.; Kwon, K.; Kim, M.; Han, S. W. *J. Phys. Chem. C* **2008**, *112*, 6717.

(44) Nitani, H.; Yuya, M.; Ono, T.; Nakagawa, T.; Seino, S.; Okitsu, K.; Mizukoshi, Y.; Emura, S.; Yamamoto, T. A. *J. Nanopart. Res.* **2006**, *8*, 951.

(45) Zhou, W.; Lee, J. Y. *Electrochem. Commun.* **2007**, *9*, 1725.

(46) Liang, H.-P.; Lawrence, N. S.; Jones, T. G. J.; Banks, C. E.; Ducati, C. *J. Am. Chem. Soc.* **2007**, *129*, 6068.

(47) Kobayashi, H.; Yamauchi, M.; Ikeda, R.; Kitagawa, H. *Chem. Commun.* **2009**, 4806.

(48) Teng, X.; Wang, Q.; Liu, P.; Han, W.; Frenkel, A.; Wen, W.; Marinkovic, N.; Hanson, J. C.; Rodriguez, J. A. *J. Am. Chem. Soc.* **2008**, *130*, 1093.

(49) Zhu, L. D.; Zhao, T. S.; Xu, J. B.; Liang, Z. X. *J. Power Sources* **2009**, *187*, 80.

(50) Hu, J. W.; Zhang, Y.; Li, J. F.; Liu, Z.; Ren, B.; Sun, S. G.; Tian, Z. Q.; Lian, T. *Chem. Phys. Lett.* **2005**, *408*, 354.

(51) Rodriguez, P.; Garcia-Araez, N.; Koper, M. T. M. *Phys. Chem. Chem. Phys.* **2010**, *12*, 9373.

(52) Moore, A.; Celorrio, V.; Montes de Oca, M. G.; Plana, D.; Hongthani, W.; Lázaro, M. J.; Fermín, D. J. *Chem. Commun.* **2011**, *47*, 7656.

(53) Hayden, B. E.; Pletcher, D.; Suchsland, J.-P.; Williams, L. *J. Phys. Chem. Chem. Phys.* **2009**, *11*, 9141.

(54) Phillips, J.; Kelly, D.; Radovic, L.; Xie, F. *J. Phys. Chem. B* **2000**, *104*, 8170.

(55) Ohba, T.; Kanoh, H.; Kaneko, K. *J. Am. Chem. Soc.* **2004**, *126*, 1560.

(56) Chu, Y. S.; Lister, T. E.; Cullen, W. G.; You, H.; Nagy, Z. *Phys. Rev. Lett.* **2001**, *86*, 3364.

(57) Fan, L. J.; Wang, C.; Chang, S. C.; Yang, Y. W. *J. Electroanal. Chem.* **1999**, *477*, 111.

(58) Zhang, G.; Wang, Y.; Wang, X.; Chen, Y.; Zhou, Y.; Tang, Y.; Lu, L.; Bao, J.; Lu, T. *Appl. Catal., B* **2011**, *102*, 614.

(59) Suo, Y.; Hsing, I. M. *Electrochim. Acta* **2011**, *56*, 2174.

(60) Zhang, X. G.; Arikawa, T.; Murakami, Y.; Yahikozawa, K.; Takasu, Y. *Electrochim. Acta* **1995**, *40*, 1889.